JOURNAL OF AIRCRAFT
Vol. 32, No. 5, September–October 1995

Experimental Investigation of Three-Dimensional Dynamic Stall Model Oscillating in Pitch

D. M. Tang* and E. H. Dowell†
Duke University, Durham, North Carolina 27708-0300

The ONERA semiempirical theoretical model for unsteady aerodynamics in the stall regime has been extended to three-dimensional flow. Parameter identification for the model is obtained from experimental dynamic stall data for a low AR rectangular wing with a NACA 0012 airfoil profile oscillating in pitch. Excellent correlations were obtained with the measured data for a three-dimensional linear aerodynamic model and reasonable agreement between theory and test data were obtained for a nonlinear (stalled) aerodynamic model. Qualitatively, the results obtained for this simple three-dimensional wing are similar to the corresponding data for the two-dimensional airfoil.

Nomenclature

b = semichord length of wing model
C_l, C_d = lift- and drag-force coefficients
C_m = moment coefficient about quarter chord
C_N, C_c = normal- and chord-force coefficients
C_p = pressure coefficient
c = chord length of wing model
D = drag force
k = reduced frequency
L = lift force
l = spanwise length
M = pitching moment, about quarter chord
p_l, p_u = lower and upper surface pressure
Re = Reynolds number, Uc/ν
t = time, s
u = velocity of a uniform flow
x, $\bar{x}$ = chordwise location, $\bar{x} = x/c$
y, $\bar{y}$ = spanwise location, $\bar{y} = y/l$
α_s = static-stall incidence, deg
ΔIm = residual imaginary transfer function for stalled aerodynamic part
Δp_i = pressure difference at ith measurement point
ΔRe = residual real transfer function for stalled aerodynamic part
θ = airfoil incidence, deg
θ_s = oscillatory amplitude, deg
θ_0 = mean incidence, deg
ν = kinematic viscosity
τ = time constant
ω = oscillatory frequency, Hz

I. Introduction

IN recent years, the state–space approach has been used effectively to study the nonlinear aeroelastic problems of aircraft wings. Since the structural dynamic model of wings and rotor blades can easily be expressed in state–space form, the same form of the unsteady aerodynamic airloads is desired. If the unsteady aerodynamic behavior can be represented by state equations, then they can be easily coupled to the structural equations of motion to construct a set of first-order ordinary differential equations (ODEs) to be solved by time-domain methods. The ONERA dynamic stall model developed by Tran and Petot[1] is a particularly useful aerodynamic model. This model describes unsteady aerodynamic forces and dynamic stall in terms of differential equations that describe the lift, drag, and moment coefficients of the section element for a one-dimensional structure. The two-dimensional incompressible aerodynamic theory was used. The aerodynamic flow variation along the spanwise direction is ignored. Therefore, the ONERA model in its present form is only usable for a large AR wing or helicopter rotor blade.

For a low AR wing, the spanwise aerodynamic variation can no longer be neglected. This is because the lifting surface may have spanwise and chordwise dimensions of the same order of magnitude, and also the spanwise and chordwise components of flow and normal stresses have nearly equal proportions. There are many linear theoretical methods for calculating the pressure distribution on a low-aspect wing in oscillatory motion in subsonic flow such as the mode function method,[2] the discrete element method,[3] and an improved doublet lattice method, i.e., the doublet-point method.[4] However, these methods are not appropriate for treating the nonlinear aeroelastic problems of low AR wings in subsonic flow.

As the need for improved nonlinear dynamics and aeroelastic analysis of the low AR wings has increased, the consequent need for unsteady dynamic stall data for three-dimensional wings has become increasingly more important. To meet these needs, an experimental investigation of a three-dimensional model undergoing pitch oscillations and dynamic stall has been performed in the Duke University low-speed wind tunnel.

Early experimental studies for oscillating two-dimensional airfoils have provided a great deal of important information on the physical mechanisms involved in dynamic stall.[1,5–10] The theoretical unsteady aerodynamic models for two-dimensional airfoils undergoing stall are semiempirically based on experimental data. The capabilities of a few commonly used unsteady aerodynamic models have been reviewed.[11]

In the present work, the main emphasis is on surface pressure measurements and construction of an unsteady aerodynamic theoretical model from these experimental data. The experimental model includes two parts: 1) a NACA 0012 wing of 10 in. chord and 15 in. span and 2) a root support mechanism with sinusoidal wing oscillation about its quarter-chord axis. The wing was vertically supported as a cantilever from the bottom of the wind tunnel. The instantaneous pressure data were obtained using a set of upper and lower pressure taps and corresponding pressure transducers at several spanwise locations extending from the tip region to the inboard

Received Sept. 22, 1994; revision received March 15, 1995; accepted for publication March 27, 1995.

*Research Associate, Department of Mechanical Engineering and Materials Science.
†Professor and Dean, School of Engineering. Fellow AIAA.

region. The integrated pressure results are presented in the body-fixed coordinate system and the resultant integrated loads represented by the pitching moment C_M and the normal-force coefficient C_N. The lift and moment coefficients C_l and C_m are expressed in terms of a set of first and second ODEs. The coefficients of these equations are determined by an improved identification technique based on experimental data obtained from fluctuating pressure signals.

The measured pressure distribution along both the chord and span is described and discussed. Comparison between steady and unsteady experimental results for both lift and pitch moment coefficients was made. The effects of spanwise position on aerodynamic behavior have been analyzed. A theoretical linear and stall aerodynamic model for a low AR wing model was constructed and its predictions examined in the light of the experimental data. The agreement between theory and measured data is excellent for the linear aerodynamic model; for the stall aerodynamic model, the agreement is reasonable though there is some contamination due to small amplitude random-like oscillations in the lift and moment of the stalled experimental data. The present identification technique needs to be further improved, although the "contamination" or noise is inherent in the turbulent flow that dynamic stall creates.

II. Description of Experiment

All steady- and unsteady-state response tests of the three-dimensional wing model were performed in the Duke University low-speed wind tunnel. The wind tunnel is a closed-circuit tunnel with a test section of 2.3×1.75 ft^2 and a length of 5 ft. The maximum airspeed attainable is 293 ft/s. The stagnation temperature of the airstream is held constant over the range 60–100°F by means of an external air exchange system, and the tunnel stagnation pressure equals atmospheric pressure at the low Reynolds number operating conditions. For the present test, the Reynolds number was 0.52×10^6 and the reduced frequency $\omega b/U$ was varied up to a value of 0.385. The wing model was constrained so that sinusoidal oscillation in pitch could be imposed about an axis passing through the quarter-chord location from the leading edge.

A. Model and Pitch Excitation

The three-dimensional NACA 0012 wing model measuring 10 in. chord, 15 in. span was mounted vertically across the test section from the tunnel floor. The wing is constructed from an aluminum alloy box spar beam with a cross section 1.5 in. wide, 0.75 in. high, and 0.125 in. thick, nine pieces of NACA 0012 airfoil plate, and an aluminum sheet 0.01 in. thick covering the entire chord and span that provides the aerodynamic contour of the wing. The pieces of the airfoil plate are made of aluminum alloy with 0.25 in. thickness and by using special manufacture. There are 20 orifices of 0.046 in. diameter for pressure taps that are symmetrically distributed over the upper and lower surfaces, respectively. The orifice positions in terms of percentage chord from the leading edge are 0.025, 0.075, 0.125, 0.2, 0.3, 0.4, 0.5, 0.6, 0.7, and 0.8. They are mounted on the box spar beam by four bolts along the wingspan of 0.9, 0.75, and 0.5 percentage span from the root to the tip of the wing. Sixty plastic tubes with 0.046 in. i.d. and connecting elements are permanently bonded on the 60 orifices of the three airfoil plates by epoxy. After installing each set of orifice and tube, they were all sealed and the sealent was sanded smooth to conform to the local airfoil contour. The 60 tubes exited the wing root through the chamber of the box spar beam and were connected to the input end of a 60/20 channels air switch. The output end of the switch is connected to 10 pressure transducers. A bracket is fixed on the root end of the box spar beam by four bolts and epoxy. The bracket is mounted on a pitch oscillatory shake table.

The pitch excitation was performed by a pitch oscillatory shake table that is mounted to a very heavy support frame that is attached to the ground. The shake table is driven using a dc servomotor through a cam. The driving frequency is controlled by a D/A NB-MIO-16 system with a Macintosh IIci computer. Also, the pitch amplitude can be adjusted. A nearly pure single harmonic excitation in the pitch direction is provided.

B. Measurement and Calibration

The static and oscillatory pressure measurements used in this test were the relative pressure between the lower and upper wing surfaces. Using a 2 ft length of plastic tubing with 0.046 in. i.d., the pressure taps on the model surface were connected to the input end of a 60/20 channel air switch located outside the tunnel. For each spanwise measurement section, there are 10 pressure measurement channels corresponding to upper and lower chordwise distributed taps. Because of the symmetrical airfoil used, the pressure difference between the upper and lower surface for a certain chordwise position is indicated by a relative pressure transducer, rather than a single-surface transducer relative to ambient pressure (atmospheric pressure). Here only 10 OMEGA PX163 pressure transducers were used in this test for measuring instantaneous pressure data of the three spanwise sections through an air switch.

The transducer measures pressure in a very low range, ± 5 in. H_2O, and features excellent sensitivity with a nominal value of 13.84 V/psi at 9 V excitation, which is much higher than the sensitivity of the miniature pressure transducer (0.01 V/psi) that was used in Ref. 8.

A 60/20 channel air switch is used to switch between spanwise measurement sections for each test. This switch has three switching positions corresponding to 90, 75, and 50% spanwise section of the wing. Experience indicates that the air leakage in the switch may be a very important problem. As shown in a leakage test, the air leakage is irregular and leads to pressure interaction between adjacent channels. After some development, a more completely sealed and reliable air-switch configuration was used in this test.

The dynamic response of the pressure tubing between the orifice on the model surface and the entrance of the air switch has been considered. When the airstream speed is less than 50 m/s and the oscillation frequency is less than 20 Hz, the dynamic effect is negligible.

Prior to testing, all pressure transducers were individually calibrated. The wind tunnel provided an exact pressure head from 0.4 in. H_2O to 2 in. H_2O, relative to local atmospheric pressure. The output data of each transducer subjected to these pressures were recorded. The calibration curves are essentially linear.

In addition to static calibrations, no-flow dynamic tests were performed at each incidence and frequency combination to obtain a dynamic calibration curve. However, the pressure sensor specification indicates that the stability, shock, and vibration behavior are suited to applications requiring exact measurement of pressure, even under dynamic conditions, and this proved to be the case.

The pitch angular displacement was measured by a rotational velocity/displacement transducer (RVDT) that is fixed at the pitch axis end of the oscillatory shake table.

The angular displacement transducer was also calibrated that showed excellent linear response characteristics (0.26%) and high sensitivity (12 deg/V).

C. Data Acquisition

The output of each pressure transducer and pitch angular displacement were directly recorded on a Macintosh IIci computer through a data acquisition package, NB-MIO-16, which consisted of a 16-channel analog-to-digital (A/D) plug-in in-

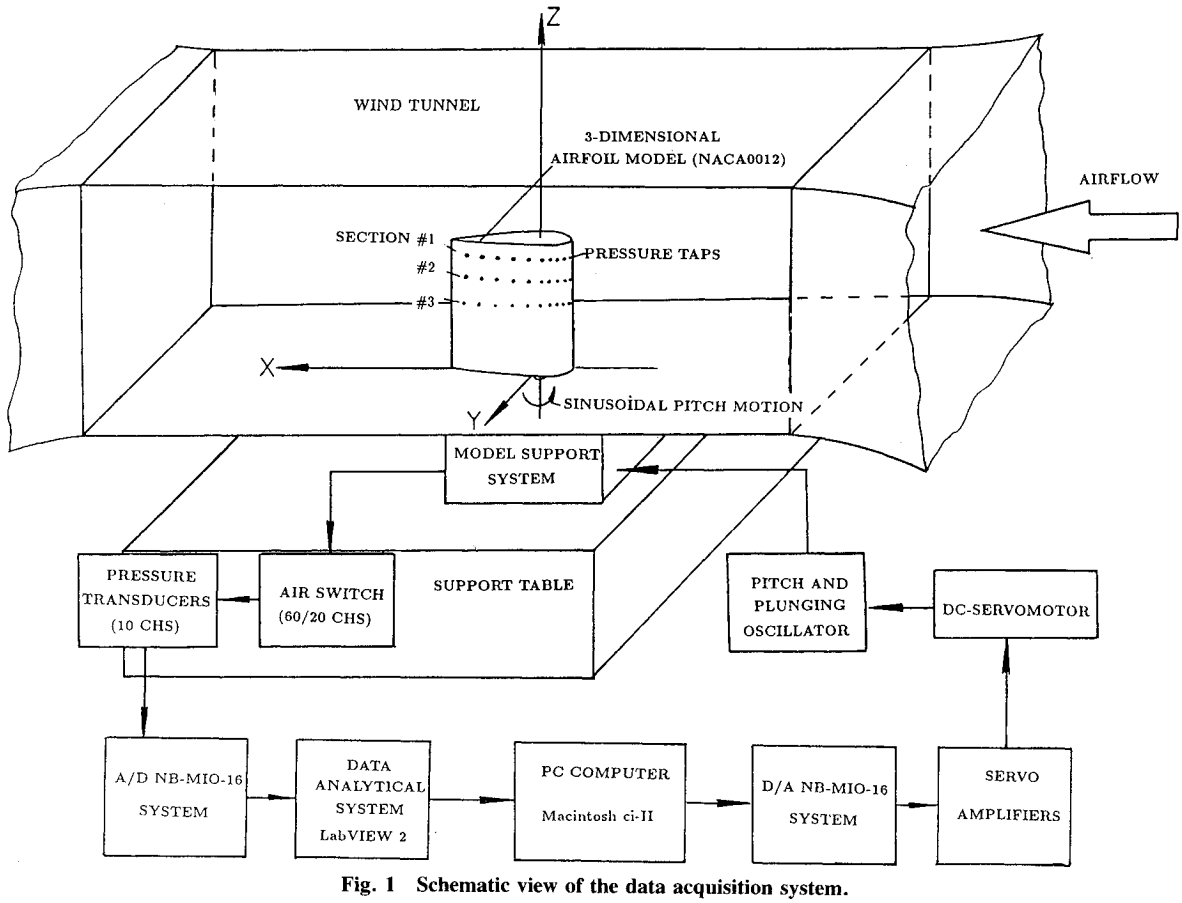

Fig. 1 Schematic view of the data acquisition system.

terface board, a BNC termination box, and data acquisition and analysis software, LabVIEW. The sampling rate (points per oscillatory cycle) was 50 points. The total number of data points was 6400. Normally, data from more than 100 cycles of wing model oscillation were recorded for reduced frequencies above 0.05. All statically calibrated data and null offset voltages of the pressure transducers at the beginning are stored in the computer for analysis. A schematic view of the data acquisition system is shown in Fig. 1.

Because of unavoidable freestream irregularities, each cycle of pressure measurements was found to be slightly different in the range below the stall angle of attack and distinctly different in the stalled portion of the cycle. In order to remove this randomness from the pressure data, an ensemble-averaging procedure over a number of cycles was carried out. The lift-force and pitching-moment coefficients are calculated by ensemble averaging the total number of recorded 100 cycles and then integration of these pressures over the airfoil.

It was observed during the course of the test that a turbulent fluctuating pressure was found at angles of attack beyond stall onset both for steady- and unsteady-state responses. It is believed to be associated with flow separation and vortex passage over the leading-edge region.[7] In this case we used a four-channel signal analyzer (SD380) to acquire the aerodynamic pressure transfer function (output pressure difference/input pitch angle) for each chordwise position on the model surface. This analyzer has an ac-coupled function and a higher data acquisition specification than that of the NB-MIO-16 package. It provides a direct measurement of the transfer function, which is defined as the ratio of the averaged cross spectrum of the input–output to the averaged input power spectrum. The reason is described in Sec. III.

III. Differential Equation Modeling of Aerodynamics

In the experimental results for a low AR wing, the aerodynamic coefficients are functions of the reduced frequency k and spanwise location y. The static lift coefficient C_{z0} is defined in two domains: 1) the linear domain, for $\theta < \alpha_s$, where $C_{z0} = a_0(y)\theta$ and 2) the stall domain. Let ΔC_z be the difference between the linear characteristic extended up to the maximum incidence and the true lift coefficient C_{z0}:

$$\Delta C_z = \begin{cases} 0 & \text{if } \theta \le \alpha_s \\ a_0(y)\theta - C_{z0} & \text{otherwise} \end{cases} \tag{1}$$

Similar to the two-dimensional ONERA linear aerodynamic model equation, these lift and pitch moment coefficients can be determined by using the following first- and second-order differential equations for a given spanwise airfoil section:

$$C_l = C_{z1} + C_{z2} + s_z t_\tau \dot{\theta} + \gamma_z t_\tau^2 \ddot{\theta} \tag{2}$$

$$t_\tau \dot{C}_{z1} + \lambda_z C_{z1} = \lambda_z a_0 \theta + t_\tau \delta_z \dot{\theta} \tag{3}$$

$$t_\tau^2 \ddot{C}_{z2} + d_z t_\tau \dot{C}_{z2} + w_z C_{z2} = -w_z \left(\Delta C_z + e_z t_\tau \frac{\partial \Delta C_z}{\partial \theta} \dot{\theta} \right) \tag{4}$$

where $t_\tau = b/u$ and the coefficients of the equations are functions of the spanwise position.

If the wing remains at low incidence, $\theta < \alpha_s$, ($\Delta C_z = 0$), one retains a linear unsteady equation [Eqs. (2) and (3)].

We now assume simple harmonic motion, i.e.,

$$\theta = \theta_s e^{ik\tau} \tag{5}$$

where $k = b2\pi\omega/u$, $\tau = ut/b$.

Substituting Eq. (5) into Eqs. (2) and (3), the transfer function for the pitch oscillations is

$$H(k) = C_l/\theta_s = \frac{\lambda_z^2 a_0 + k^2 \delta_z}{\lambda_z^2 + k^2} - \gamma_z k^2 + ik \frac{\lambda_z(\delta_z - a_0) + (\lambda_z^2 + k^2)s_z}{\lambda_z^2 + k^2} \tag{6}$$

The measured aerodynamic transfer function is expressed as

$$H(k) = \mathrm{Re}_1(k) + i\,\mathrm{Im}_1(k)$$

Because of the simple harmonic motion of both input and output signals, the measured aerodynamic transfer function is determined from the ratio C_l/θ_s of the output to input amplitude and the phase shift ψ between output and input signals. That is,

$$\mathrm{Re}_1(k) = |C_l/\theta_s|\cos\psi \tag{7}$$

$$\mathrm{Im}_1(k) = |C_l/\theta_s|\sin\psi \tag{8}$$

A Gauss–Newton method, or a nonlinear least-square curve-fitting program is used to determine the coefficients, λ_z, δ_z, a_0, s_z, and γ_z.

If the wing is at high incidence, $\theta > \alpha_s$, ($\Delta C_z \neq 0$), a stall nonlinear unsteady equation [Eq. (4)] must be considered. The coefficients d_z, w_z, and e_z can be obtained using an identification technique of the model through tests at small amplitude motions. For small amplitude ($\theta_s \leq 1$ deg) sinusoidal pitch oscillation of the model, the aerodynamic responses approach a sinusoidal shape, even in the stall regime. Indeed, the relative amplitudes of the higher harmonics are negligible in the whole range of mean incidences θ_0 and reduced frequencies k of the test. This property is important in the identification process.

The residual real and imaginary components of the aerodynamic transfer function for the stall equation part are defined as

$$\Delta\mathrm{Re}(k) = \mathrm{Re}(k, \theta_0)_{\mathrm{test}} - \mathrm{Re}_1(k, \theta_0) = \left[\frac{w_z \dfrac{d\Delta C_z}{d\theta}}{(k^2 - w_z^2)^2 + (d_z k)^2}\right][k^2(1 - d_z e_z) - w_z]_{\theta_0} \tag{9}$$

$$\Delta\mathrm{Im}(k) = \mathrm{Im}(k, \theta_0)_{\mathrm{test}} - \mathrm{Im}_1(k, \theta_0) = k\left[\frac{w_z \dfrac{d\Delta C_z}{d\theta}}{(k^2 - w_z^2)^2 + (d_z k)^2}\right][e_z(k^2 - w_z) + d_z]_{\theta_0} \tag{10}$$

where $\mathrm{Re}_1(k, \theta_0)$ and $\mathrm{Im}_1(k, \theta_0)$ are determined using the identified parameters from the linear unsteady aerodynamic equations.

In fact the measured real and imaginary parts, $\mathrm{Re}(k, \theta_0)_{\mathrm{test}}$ and $\mathrm{Im}(k, \theta_0)_{\mathrm{test}}$, include the aerodynamic pressure noise due to a stalled unsteady state. The measured data show that the input can be regarded as a pure sinusoidal signal and the noise is only involved in the output pressure signal. Thus, this method needs to be modified, as described next.

Let the aerodynamic noise be a stationary random process with a zero-average value, defined as $\eta(t)$. The output pressure difference on the wing surface and the input pitch angle can be represented as

$$\Delta p(t) = \Delta p_0(t) + \eta(t)$$

$$\theta(t) = \theta_0 + \theta_s \sin(2\pi\omega t)$$

The aerodynamic transfer function, $H(k)$ is defined as the ratio of the cross power spectral density (PSD) of output-input, to the auto PSD of the input

$$H(k) = \frac{S_{p\theta}(k)}{S_{\theta\theta}(k)} = \frac{\tilde{S}_{p\theta}(k) + \Delta S_{p\theta\eta}(k)}{\tilde{S}_{\theta\theta}(k)} \tag{11}$$

where $S_{\theta\theta}(k)$, $S_{pp}(k)$, and $S_{p\theta}(k)$ are the measured auto-PSD of the input, output, and the cross-PSD; and $\tilde{S}_{\theta\theta}(k)$, $\tilde{S}_{pp}(k)$, and $\tilde{S}_{p\theta}(k)$ are the corresponding true values of PSD. $S_\eta(k)$ and $\Delta S_{p\theta\eta}(k)$ are the noise auto- and cross-PSD.

If the aerodynamic noise is independent of the input and output signals, the term, $\Delta S_{p\theta\eta}(k)$, of the noise cross PSD should be zero. If the aerodynamic noise is dependent of the input and output signals, increasing the ensemble-averaging number will effectively reject noise.

This procedure is also suited for the moment coefficient C_m, in which the subscript z of the previous equations and the coefficients is replaced by m.

IV. Steady-State Results

Steady test data have been presented as lift, drag forces, and pitch moment about the quarter chord in terms of normal and chordwise components in a fixed coordinate system. The measured pressure coefficient C_p response vs incidence angle from 2 to 28 deg and various chordwise locations for several spanwise locations were made. A typical example for $\bar{y} = 0.75$ is shown in Fig. 2. The freestream velocity is 20.56 m/s. C_p is defined as the pressure difference Δp between upper and lower surfaces divided by the freestream dynamic pressure q. It was found that the maximum pressure difference is located at $\bar{x} = 0.025$ and decreases as $\bar{x}$ increases up to the trailing edge of the wing model. When the incidence angle is less than 16 deg (i.e., the static stall angle, $\alpha_s = 16$ deg), the data were quite smooth and repeatable. When it is greater than α_s there is a large scatter in the pressure measurement, especially in the range of the leading edge. The data plotted in Fig. 2 are average values for large incidence. The turbulent pressure due to the airflow separation at the leading edge is characterized by a von Kármán spectrum with zero mean value.

The spanwise effect on the measured pressure distribution for unstalled and stalled state was found. For the unstalled case, the pressure distribution approaches that of a two-dimensional airfoil when the spanwise location varies from the tip region to the inboard region. At $\bar{y} = 0.9$ (near tip), the pressure difference near the trailing edge has a distinct variation, i.e., it becomes larger at $\bar{x} = 0.7$, and smaller at $\bar{x} = 0.8$. This is because there is a reverse flow near the wingtip. For the stalled case, the previous phenomenon is also existent and the high pressure at the leading edge decreases. The pressure distribution along the chord becomes flatter than for the unstalled case.

Figures 3–5 show the lift, drag, and pitch moment coefficients for three spanwise locations. All chordwise data show excellent repeatability for an incidence angle lower than 16 deg. However, for a higher angle of incidence the data appear to be seriously contaminated by the turbulent aerodynamic noise. We use a bar in these figures to indicate the fluctuation

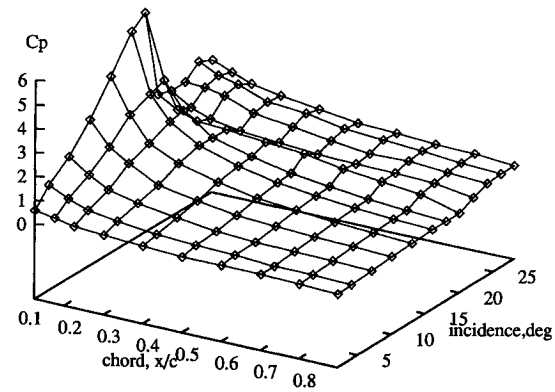

Fig. 2 Steady pressure coefficients chordwise distribution vs incidence for $\bar{y} = 0.75$.

magnitude of the pressure variation. The local static lift-curve slope $[a_0(y) = C_l(y)/\theta]$ are 2.87, 3.61, and 4.02 at $\bar{y} = 0.9$, 0.75, and 0.5, which differs substantially from the results for the two-dimensional NACA 0012 airfoil. It is believed that when $\bar{y} \to 0$, the lift-curve slope approaches 5.73, and when $\bar{y} \to 1$, the lift-curve slope approaches 0.

The stalled irregular patterns appearing in both the forces and moment coefficients are similar to those from the two-dimensional results of earlier investigators. For convenient application a formula for the stalled lift coefficient $C_{z0}(y)$ is constructed

$$C_{z0}(y) = \sum_{i=0}^{4} c_i(\theta - \alpha_s)^i \tag{12}$$

where $c_0, \ldots c_4$ are determined by the least-square curve-fitting method. The results are listed in Table 1.

The lift coefficient can be expressed as

$$C_l(y) = \begin{cases} a_0(y)\theta & \text{if } \theta < 16 \text{ deg} \\ C_{z0}(y) & \text{otherwise} \end{cases} \tag{13}$$

For the pitch moment coefficient, it is expressed as

$$C_m(y) = \begin{cases} b_0(y) + b_1(y)\theta & \text{if } \theta < 16 \text{ deg} \\ b_2(y) + b_3(y)(\theta - 18 \text{ deg}) & \text{if } \theta > 18 \text{ deg} \\ b_4(y) + b_5(y)(\theta - 16 \text{ deg}) & \text{if } 18 \text{ deg} \geq \theta \geq 16 \text{ deg} \end{cases} \tag{14}$$

where $b_0, b_1 \ldots$ are listed in Table 2.

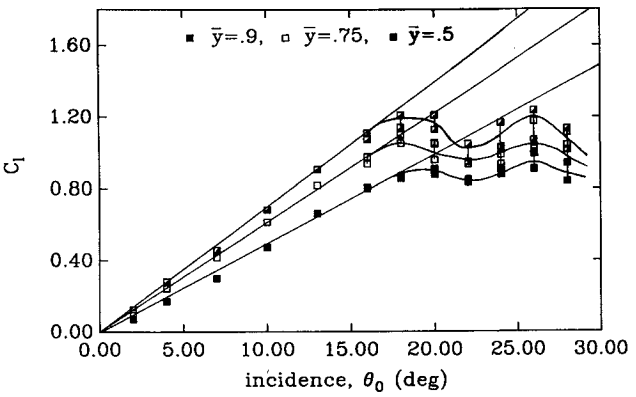

Fig. 3 Static lift coefficient vs incidence angle.

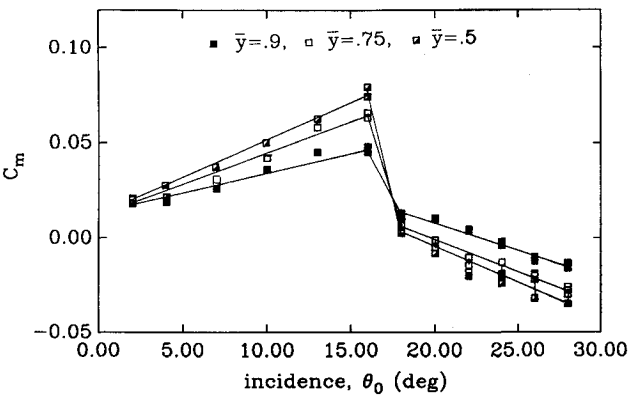

Fig. 4 Static pitch moment coefficient vs incidence angle.

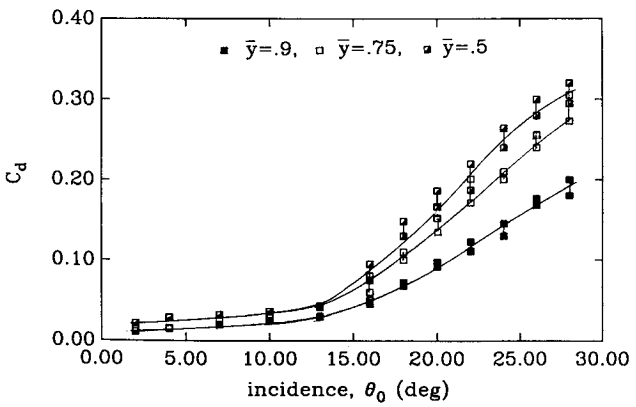

Fig. 5 Static drag coefficient vs incidence angle.

V. Unsteady-State Results

The unsteady aerodynamic response data were acquired from an oscillating wing model. The oscillatory frequency varied from 2 to 14 Hz with the pitch amplitudes, $\theta_s = 1$, 3, and 6 deg. The airstream velocities are 20.56 and 28.51 m/s. The measured unsteady response data included two parts: 1) unstalled and 2) stalled data. These data were used to identify and construct the linear and nonlinear (stall) aerodynamic model, i.e., a set of differential equations for a low AR wing model. The effect of spanwise aerodynamic forces is modeled in the aerodynamic coefficients in these equations.

A. Unstalled Aerodynamic Responses

A typical example of the unsteady pressure time history (one oscillatory cycle) obtained in this test is shown in Fig. 6 for a mean incidence angle $\theta_0 = 9$ deg, $\theta_s = 6$ deg, $\omega = 4$ Hz, $k = 0.17$, and $\bar{y} = 0.75$ (it is not shown for $\bar{y} = 0.9$ and 0.5). In this figure, the maximum response trace was located at the first chordwise station at $x = 0.025$. The motion is sinusoidal. The response amplitude decays with increasing $\bar{x}$. The minimum response is located at $\bar{x} = 0.7$ for $\bar{y} = 0.9$ and at $\bar{x} = 0.8$ for $\bar{y} = 0.75$ and 0.5. The reason for this behavior has been discussed previously in Sec. IV. For response traces corresponding to different chordwise stations, there is a slight phase shift relative to the first chordwise station.

The integrations of the chordwise pressure distribution were performed after verifying the cycle-to-cycle repeatability of the individual pressure transducer responses. A cycle-averaging procedure was used to smooth the pressure signals, in order to obtain a mean representation of the cyclical lift and

Table 1 Polynomial coefficients for static lift coefficient

$\bar{y}$	c_0	c_1	c_2	c_3	c_4
0.90	0.8032	0.05909	−0.01952	0.00282	−0.00013
0.75	0.9772	0.14810	−0.07468	0.01084	−0.00047
0.50	1.0747	0.17609	−0.08652	0.01135	−0.00045

Table 2 Polynomial coefficients for pitch moment coefficient

$\bar{y}$	b_0	b_1	b_2	b_3	b_4	b_5
0.90	0.0114	0.00228	0.01582	−0.00389	0.04711	−0.015610
0.75	0.00774	0.00372	−0.01036	−0.00243	0.06722	−0.038790
0.50	0.00699	0.00407	−0.00924	−0.00202	0.07211	−0.040675

Table 3 Coefficients of linear aerodynamic equation

$\bar{y}$	a_0	λ_z	δ_z	γ_z	s_z
0.90	2.87	0.0469	2.4050	23.5012	−3.7797
0.75	3.61	0.0772	3.0121	21.1647	−4.6957
0.50	4.02	0.0973	3.4126	17.49	−5.928

Table 4 Coefficients of stalled aerodynamic equation

$\bar{y}$	b_0	λ_m	δ_m	γ_m	s_m
0.90	0.13	0.0108	0.0053	1.1329	−0.3261
0.75	0.21	0.117	0.0192	1.5403	−0.4515
0.50	0.23	0.121	0.0879	1.9907	−0.6065

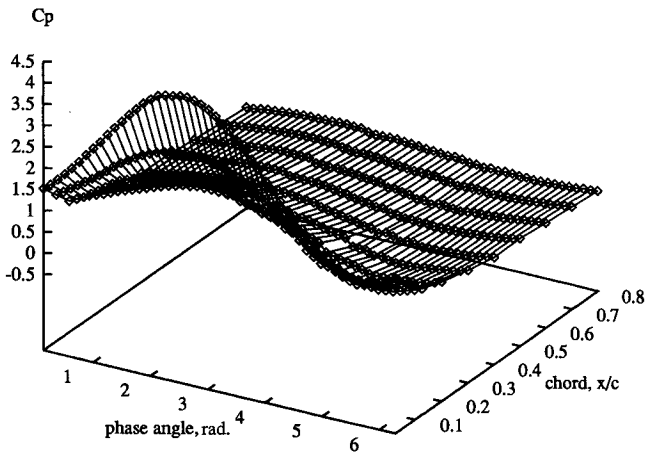

Fig. 6 Unsteady pressure coefficient chordwise distribution vs time for θ_0 = 9 deg, θ_s = 6 deg, ω = 4 Hz, k = 0.17 and $\bar{y}$ = 0.75.

moment responses. In order to obtain a good signal/noise ratio (SNR) for identifying linear unsteady equations, a larger excitation amplitude is used in the test. The reduced frequency varies from k = 0.08 to 0.35. The other parameters are θ_0 = 9 deg, u = 20.56 m/s, θ_s = 6 deg, and $\bar{y}$ = 0.5, 0.75, and 0.9. From these data, the real and imaginary parts of aerodynamic transfer function relative to the input pitch oscillation can be determined. The results obtained by a nonlinear least-square curve fitting method using several reduced frequency data are listed in Tables 3 and 4.

Figure 7 shows the aerodynamic transfer functions of the unsteady aerodynamic forces as they vary with reduced frequency k. In these figures, a) is for the real component and b) is for the imaginary component for different spanwise stations $\bar{y}$ = 0.9, 0.75, and 0.5. The theoretical curves in Fig. 7 are obtained from Eq. (6) in which the coefficients are determined by a nonlinear least-square curve-fitting program from a number of experimental data (k = 0–0.385). The static experimental data $\alpha_0(y)$ for k = 0 are the constrained conditions for the present curve-fitting program. The agreement between theory and experiment is good.

From the cycle-averaged time histories of lift and pitch moment coefficients and pitch excitation signal, we can obtain the lift and moment hysteresis loop plots. A typical theoretical and experimental lift and moment hysteresis loop plots are shown in Fig. 8 corresponding to θ_0 = 9 deg, θ_s = 6 deg at $\bar{y}$ = 0.75 and a higher reduced frequency k = 0.35. A quantity that represents the degree of hysteresis is given by the pitch aerodynamic damping ξ. It is defined as

$$\xi = -\oint C_m \, d\theta/\pi\theta_s^2 \tag{15}$$

The pitch aerodynamic damping term represents the transfer of energy between the wing pitching motion and the surrounding unsteady flow environment. When ξ is positive, the airstream makes the wing pitch motion stable. Conversely, a negative value of ξ represents unstable motion. From these hysteresis loop plots, it is found that near the inboard portion of the wing, there is a larger positive aerodynamic pitch damping.

The pitch aerodynamic damping parameter ξ was determined by performing a Fourier analysis of the measured pitch

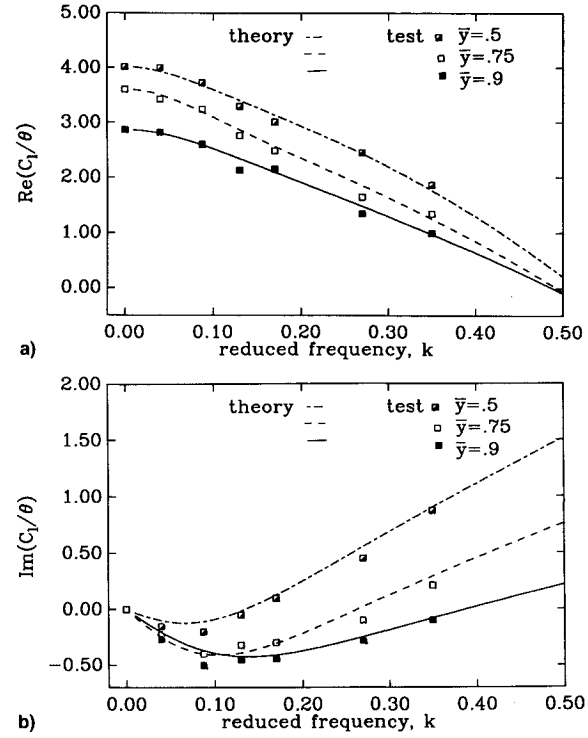

Fig. 7 Lift transfer function of unsteady aerodynamic force vs reduced frequency for a) real and b) imaginary parts.

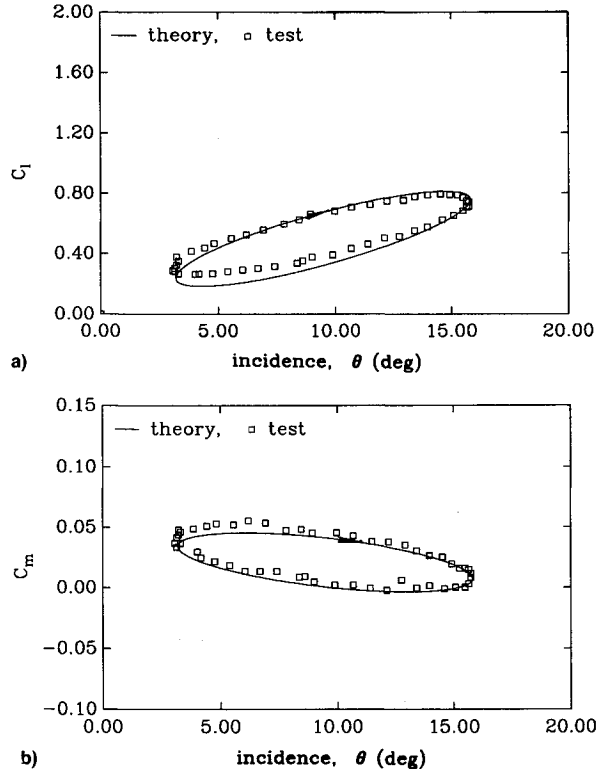

Fig. 8 Hysteresis loop plots for θ_0 = 9 deg, θ_s = 6 deg, k = 0.35 at $\bar{y}$ = 0.90 for a) lift and b) moment.

moment response and then substituting the first harmonic component into Eq. (15). Figure 9 shows the variation of aerodynamic damping parameter vs k for $\theta_0 = 9$ deg, $\theta_s = 6$ deg, and $\bar{y} = 0.5, 0.75$, and 0.9. The damping values increase with increasing reduced frequency, but do not have the linear relationship with k as predicted in the two-dimensional linear aerodynamic theory ($\xi = k\pi/2$), see Ref. 12.

As shown in Fig. 9, the effects of the spanwise location on damping are not neglected. ξ decreases as the spanwise location moves from the inboard region to the tip of the wing. The results for $\bar{y} = 0.5$ are slightly closer to the theoretical values obtained from two-dimensional linear prediction than those for $\bar{y} = 0.75$ and 0.9.

B. Stalled Aerodynamic Responses

During the previous steady test, static stall behavior has been observed. When the mean incidence angle of the oscillating wing model is greater than the static stall angle, the unsteady aerodynamic behavior is characterized by stalled nonlinear aerodynamics. The aerodynamic responses have a more complex shape and depend upon the mean incidence angle. Following Fig. 6, when the mean incidence angle is $\theta_0 = 21$ deg rather than 9 deg, the time histories of unsteady pressure at each transducer station are shown in Fig. 10 for $\bar{y} = 0.75$ (it is not shown for $\bar{y} = 0.5$ and 0.9). By comparison of Fig. 10 with Fig. 6, although the single harmonic motion of the pressure distribution has disappeared, there is still periodic motion, but now with multiple harmonic components. The dominant frequency component is 5.87 Hz, that is identical with the pitch excitation frequency. The pressure distribution along the chord becomes flatter. The pressure variation near the trailing edge at $\bar{y} = 0.9$ has a substantial distortion from the unstalled case. The reverse flow at the tip of wing model becomes stronger than that for small incidence angle. The magnitude at $\bar{x} = 0.8$ is larger than that at $\bar{x} = 0.7$ for the entire cycle.

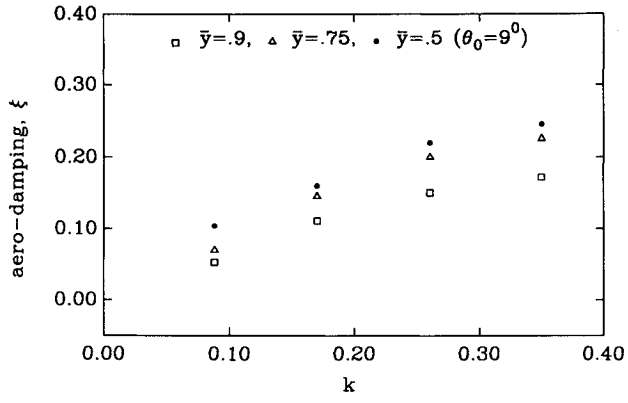

Fig. 9 Variation of aerodynamic damping with reduced frequency for $\theta_0 = 9$ deg, $\theta_s = 6$ deg, at $\bar{y} = 0.5, 0.75$, and 0.9.

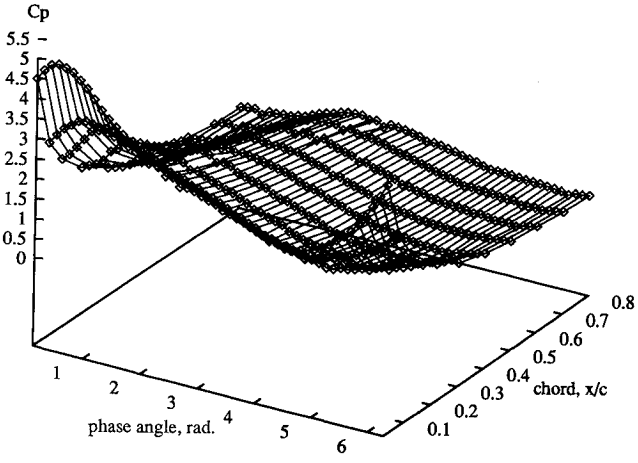

Fig. 10 Unsteady pressure coefficient chordwise distribution vs time for $\theta_0 = 21$ deg, $\theta_s = 6$ deg, $\omega = 4$ Hz, and $k = 0.17$. For $\bar{y}$ = a) 0.9, b) 0.75, and c) 0.5.

From the measured stalled response data, the comparison of the pressure distribution along the span at the first chordwise station $\bar{x} = 0.025$ was made. The resultant amplitude at $\bar{y} = 0.5$ is larger than that at $\bar{y} = 0.9$ and decreases with increasing $\bar{y}$. The relative position for maximum and minimum pressure point in one cycle varies with the span. This means the phase shift relative to the pitch oscillation for the dominant component increases with decreasing $\bar{y}$. Also, the stall behavior of the time histories of the averaged cyclical lift and pitch moment coefficients vs the several mean incidence angles, $\theta_0 = 9$, 13, 18, and 21 deg, for $k = 0.088$, $\theta_s = 6$ deg, $u = 20.56$ m/s, and $\bar{y} = 0.5, 0.75$, and 0.9 was observed. The evolution process for the stalled aerodynamic response from a single harmonic motion to a periodic motion is clearly found. At $\theta_0 = 13$ deg, the true incidence angle is partially involved in the unstalled and stalled portions for a whole cycle pitch motion. The 5.87-Hz frequency component is more dominant than at $\theta_0 = 18$ and 21 deg. The lift response approaches to a single harmonic motion. Although there is a larger pressure variation near the trailing edge at $\bar{y} = 0.9$ due to the onset of stall, the lift coefficient variation along the span is not significantly different from the unstalled case. This is because the contribution of trailing-pressure distribution to the lift coefficient is smaller than the major pressure in the leading-edge region. However, in contrast to the lift coefficient, the pitch moment coefficient (about the quarter chord) is quite sensitive to the chordwise pressure distribution. The moment response appears to have a stronger nonlinearity beginning at $\theta_0 = 13$ deg, especially for the $\bar{y} = 0.9$ position. The moment response is much more complex than those for $\bar{y} = 0.75$ and 0.5. Due to the small scale the moment curve is not very smooth as compared with the lift curve.

The identification of the stalled nonlinear differential equation based on Eq. (9) and Eq. (10) is very difficult due to the small amplitude motion and the contamination from the aerodynamic noise. As mentioned previously, an improved data acquisition method is used to obtain the real and imaginary components of the aerodynamic transfer function for small amplitude motion in the stall regime.

A typical example of the time histories of unsteady pressure response obtained in this test is shown in Fig. 11 for $\theta_s = 1$ deg and several mean incidence angles, $\theta_0 = 9$, 13, 16, 20, 23, 26, and 28 deg. Other test parameters were $u = 20.56$ m/s, $\omega = 5.87$ Hz, $k = 0.237$, $\bar{y} = 0.5$, and $\bar{x} = 0.075$. In this figure the top trace is for $\theta_0 = 28$ deg. At the bottom of the figure is the angular displacement time history relative to the mean incidence angle.

In the region of low mean incidence angle $\theta_0 < 16$ deg, the responses are essentially simple single harmonic motion without noise contamination. The response amplitudes are identical for different mean incidence angle as shown in traces of $\theta_0 = 9$ and 13 deg. When $\theta_0 = 16$ deg, the response amplitude decreases, but the motion retains a sinusoidal pattern. The random noise is small. From $\theta_0 = 20$–28°, the signals are contaminated by the aerodynamic noise due to stall. The degree of contamination increases with increasing mean incidence angle. From the PSD plots, it is found that at $\theta_0 = 13$ deg, the background noise is negligible and the SNR reaches above 40 dB. At $\theta_0 = 26$ deg, the background noise is significant and the SNR is only about 20 dB.

Using Eq. (11), the pressure transfer function was substantially improved after ensemble averaging over 200 realizations. From a typical example, $\bar{x} = 0.075$, $\bar{y} = 0.5$, $k = 0.17$, $\theta_0 = 21$ deg, and $\theta_s = 1$ deg, it is found that the turbulent random noise in the real and imaginary components of the

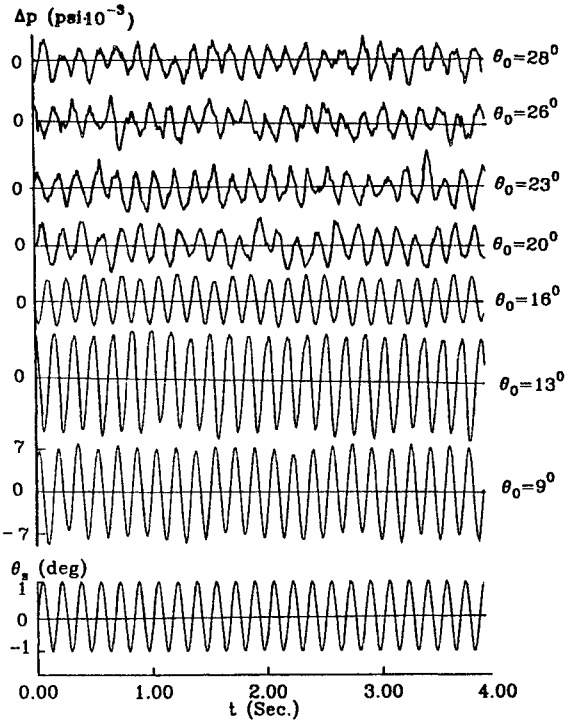

Fig. 11 Pressure time histories vs incidence angles for u = 20.56 m/s, θ_s = 1 deg, ω = 5.87 Hz, k = 0.237 at $\bar{y}$ = 0.5 and $\bar{x}$ = 0.075.

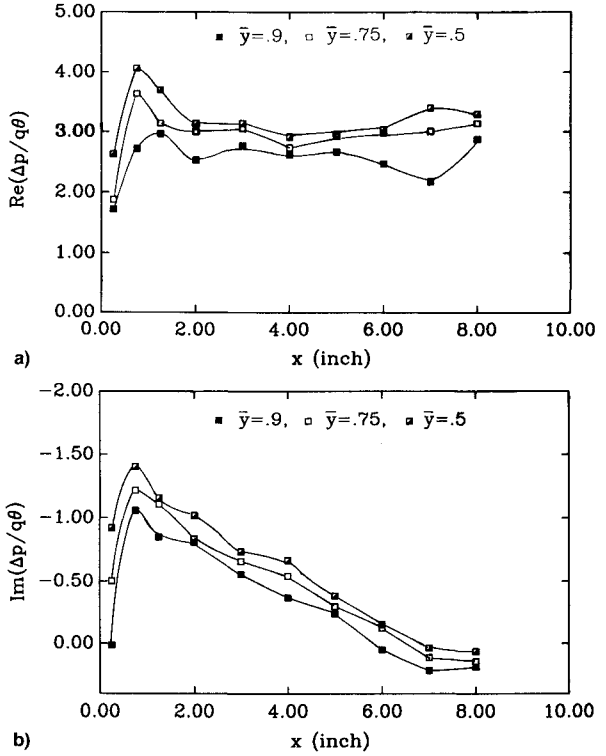

Fig. 12 Pressure transfer function vs chordwise locations for θ_0 = 23 deg, θ_s = 1 deg, k = 0.224: a) for real part and b) for imaginary part.

pressure transfer function is mostly rejected as the average number increases up to 200.

Figure 12 shows the real and imaginary pressure distribution of the aerodynamic transfer function for θ_0 = 23 deg, θ_s = 1 deg, k = 0.224 at $\bar{y}$ = 0.9, 0.7, and 0.5. Similar to the results obtained for larger amplitude excitation at high mean incidence angle, the pressure distribution along the chord is flatter than for small θ_0. The maximum pressure amplitude at the leading edge decreases and the trailing-pressure amplitude increases. From different k values, k = 0.079, 0.118, 0.158, 0.197, 0.237, 0.275, 0.316, and θ_0 = 23 deg, θ_s = 1 deg, we can obtain a set of measured data to identify the stalled aerodynamic model using Eqs. (9) and (10).

The residual transfer functions for the stalled part, $\Delta\mathrm{Re}(C_l/\theta)$ and $\Delta\mathrm{Im}(C_l/\theta)$, vs reduced frequency k are shown in Fig. 13. For θ_0 = 23 deg, $(\mathrm{d}\Delta C_z/\mathrm{d}\theta)$ is 1.616, 0.6747, and 2.369

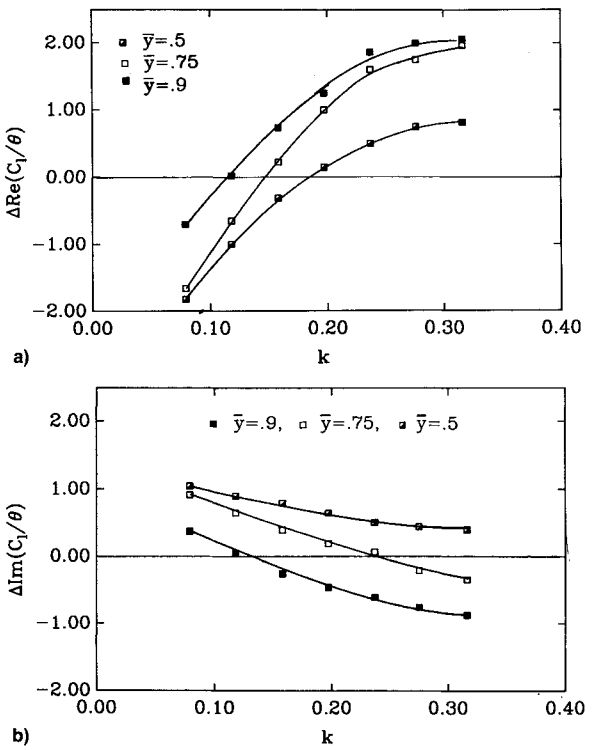

Fig. 13 Lift residual transfer function vs k for θ_0 = 23 deg, θ_s = 1 deg: a) for real residual part and b) for imaginary residual part.

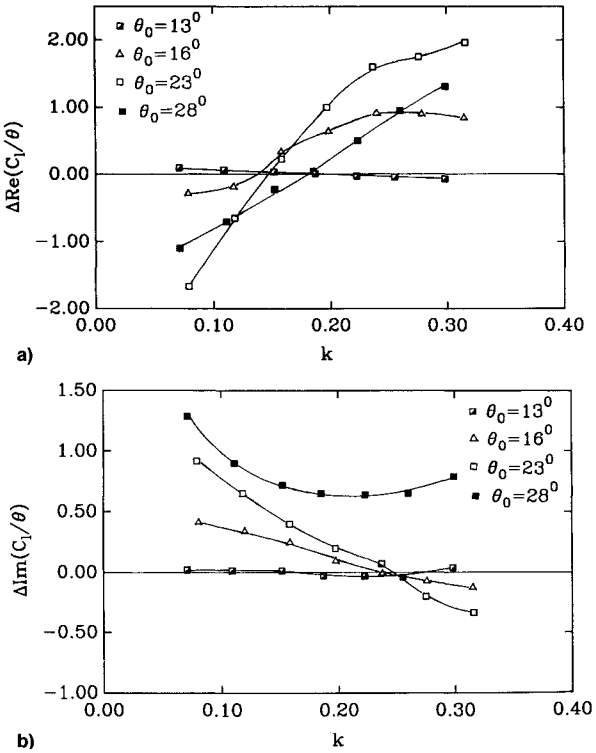

Fig. 14 Lift residual transfer function vs k for θ_s = 1 deg and several θ_0 at $\bar{y}$ = 0.75: a) for real residual part and b) for imaginary residual part.

at $\bar{y}$ = 0.9, 0.75 and 0.5, respectively. There are some special points in Fig. 13a that are very useful for solving the nonlinear least-squares equation. The points corresponding to $\Delta\text{Re}(C_l/\theta) = 0$ are k_{el} = 0.11, 0.145, and 0.185 for $\bar{y}$ = 0.9, 0.75, and 0.5, respectively.

For other mean incidence angles, θ_0 = 13, 16, 23, and 28 deg, the stalled transfer functions are also measured. The results are shown in Fig. 14 for $\bar{y}$ = 0.75. When θ_0 = 13 deg there is no onset of stall, the residual real and imaginary components of lift for the stalled part are almost zero. The residual values of ΔRe and ΔIm increase with increasing θ_0. These measured data were also used to identify the stalled aerodynamic model equation. The results are shown in Fig. 15, which display the coefficients, w_z, d_z, and e_z in the stall equation vs the mean incidence angle. From these figures, it is found that the typical coefficient is a nonlinear function of mean incidence angle, i.e., it depends on the static lift coefficient difference ΔC_z. As compared with the results from two-dimensional airfoil, the general trend is the same, but there is a quantitative difference due to different static lift behavior.

To assess the ability of the generalized ONERA model to predict aerodynamic response for large motions (θ_s = 6 deg) based upon coefficients determined from small motion (θ_s = 1 deg), consider the following. Some typical stalled hysteresis loop plots are shown in Figs. 16 and 17 for θ_0 = 23 deg, θ_s = 6 deg at $\bar{y}$ = 0.75, and k = 0.088 and 0.35. For the lower reduced frequency, there is a "∞" pattern hysteresis loop both for the lift and moment coefficients as shown in Fig. 16. The negative and positive aerodynamic damping are alternatively generated in a cyclical pitch oscillation. The agreement be-

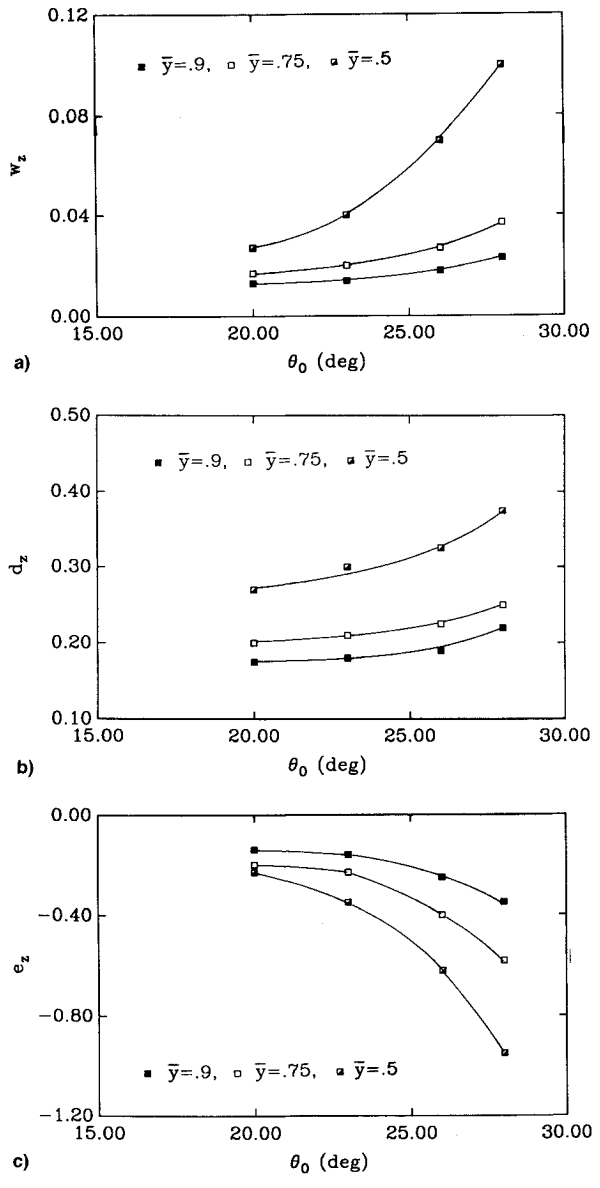

Fig. 15 Coefficients of stalled lift equation vs incidence angles for a) w_z, b) d_z, and c) e_z.

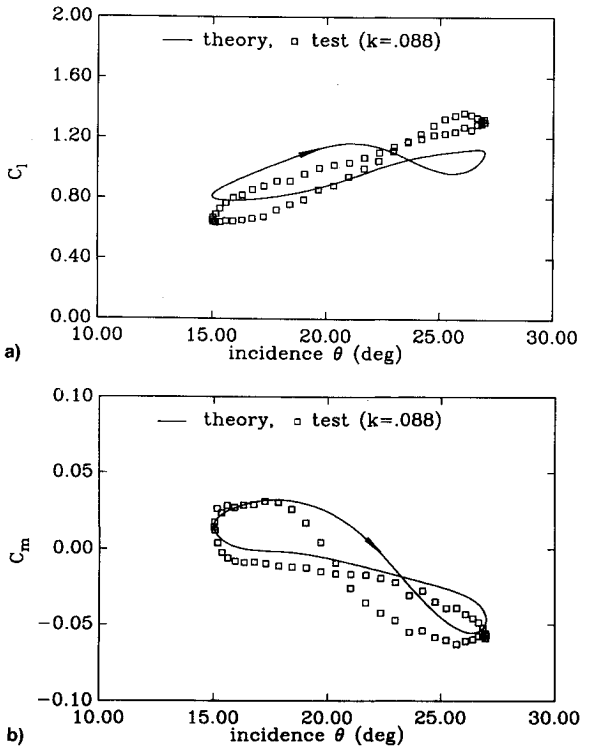

Fig. 16 Hysteresis loop plots for θ_0 = 23 deg, θ_s = 6 deg, k = 0.088 at $\bar{y}$ = 0.75 for a) lift and b) moment.

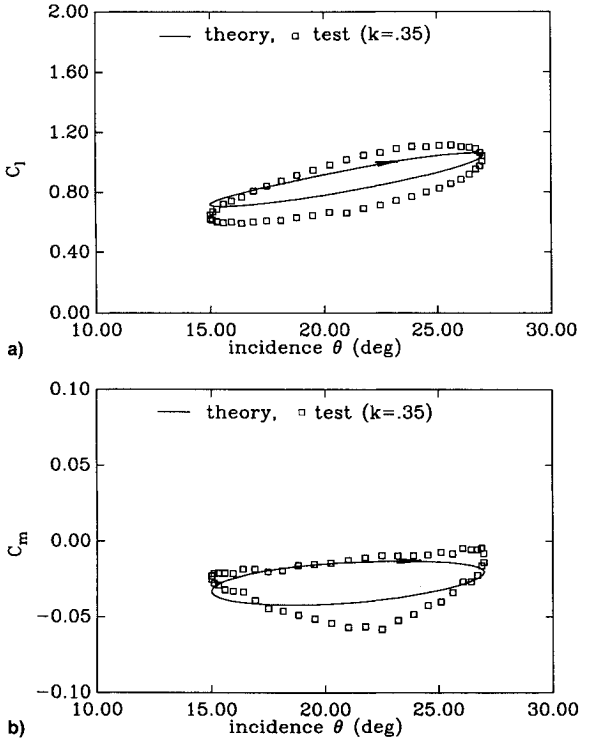

Fig. 17 Hysteresis loop plots for θ_0 = 23 deg, θ_s = 6 deg, k = 0.35 at $\bar{y}$ = 0.75 for a) lift and b) moment.

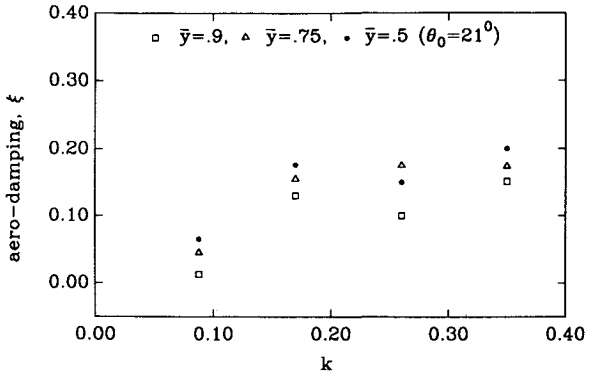

Fig. 18 Variation of aerodynamic damping with reduced frequency for θ_0 = 21 deg, θ_s = 6 deg at $\bar{y}$ = 0.5, 0.75, and 0.9.

tween theory and experiment is reasonable, but not perfect. This is because the present identification method is based on the small amplitude motion. The measured data used in the identifying process were seriously contaminated by aerodynamic noise due to stall. The input data with a smaller SNR will lead to a larger identification error. The identification technique for the stall aerodynamic model needs to be further improved.

In terms of these measured moment loop plots, the aerodynamic damping for the stalled case is also determined. Differing from the method in Fig. 9, we directly use a loop integration to obtain a hysteresis area. The area enclosed by the clockwise traversed path provides a positive damping and by the counterclockwise subloop provides a negative damping. The resultant damping is proportional to the area difference between these two.

In contrast to the unstalled case, as shown in Fig. 9, Fig. 18 shows the variation of aerodynamic damping parameter vs k for θ_0 = 21 deg, θ_s = 6 deg, and $\bar{y}$ = 0.5, 0.75, and 0.9. The damping values are substantially influenced by the reduced frequency and mean incidence angle. The damping does not have a general variation rule with increasing k and θ_0. In a typical example shown in Fig. 18, the damping reaches a minimum value at k = 0.088 and approaches zero at $\bar{y}$ = 0.9. The magnitude of the damping is smaller than that for the unstalled case. The qualitative trend of ξ with $\bar{y}$ seems to be consistent with Fig. 9.

VI. Conclusions

An experimental investigation of three-dimensional unstalled and stalled aerodynamic behavior has been conducted for a low AR wing model. The measured pressure distribution data on the wing model surface along both the chord and span are used to construct an unsteady stall aerodynamic model. The results lead to the following conclusions:

1) The ONERA semi-empirical model for unsteady aerodynamics in the stall regime has been extended to three-dimensional flow.

2) A substantial body of unsteady aerodynamic experimental data has been obtained that will be useful in evaluating the ONERA model as well as other aerodynamic models for three-dimensional stalled and unstalled flow.

3) Qualitatively, the results obtained for this simple three-dimensional wing are similar to the corresponding data for the two-dimensional airfoil.

4) It would be of interest to extend these measurements and modeling to higher speed flow and more complicated wing planforms.

Acknowledgments

This work was supported by the Air Force Office of Scientific Research under Grant F 49620-93-1-0420. C. I. "Jim" Chang is the Technical Monitor.

References

[1]Tran, C. T., and Petot, D., "Semi-Empirical Model for the Dynamic Stall of Airfoils in View to the Application to the Calculation of Responses of a Helicopter Blade in Forward Flight," *Vertica*, Vol. 5, May 1981, pp. 35–53.

[2]Watkin, C. E., Woolston, D. S., and Cunningham, H. J., "A Systematic Kernel Function Procedure for Determining Aerodynamic Forces on Oscillating or Steady Finite Wings at Subsonic Speed," NASA TR R-48, July 1959.

[3]Landahl, M. T., and Stark, J. E., "Numerical Lifting-Surface Theory—Problems and Progress," *AIAA Journal*, Vol. 6, No. 11, 1968, pp. 2049–2060.

[4]Ueda, T., and Dowell, E. H., "A New Solution Method for Lifting Surfaces in Subsonic Flow," *AIAA Journal*, Vol. 20, No. 3, 1982, pp. 348–355.

[5]Liiva, J., Davenport, F. J., Grey, L., and Walton, I. C., "Two-Dimensional Tests of Airfoils Oscillating Near Stall," U.S. Army Aviation Material Labs. TR-68-13, April 1968.

[6]Carta, F. O., "Analysis of Oscillatory Pressure Data Including Dynamic Stall Effects," NASA CR-2394, May 1974.

[7]Carr, L. W., McAlister, K. W., and McCroskey, W. J., "Dynamic Stall Experiments on the NACA 0012 Airfoil," NASA TP-1100, Dec. 1978.

[8]Hilaire, A. O., and Carta, F. O., "Analysis of Unswept and Swept Wing Chordwise Pressure Data from an Oscillating NACA 0012 Airfoil Experiment," Vol. 1, TR NASA CR 3567, March 1983.

[9]Hilaire, A. O., and Carta, F. O., "Analysis of Unswept and Swept Wing Chordwise Pressure Data from an Oscillating NACA 0012 Airfoil Experiment," Vol. 2, Data Rept., NASA CR 165927, June 1983.

[10]McCroskey, W. J., McAlister, K. W., Carr, L. W., and Pucci, S. L., "An Experimental Study of Dynamic Stall on Advanced Airfoil Sections, Volume 1, Summary of the Experiment," NASA TM 84245, July 1982.

[11]Reddy, T. S. R., and Kaza, K. R. V., "A Comparative Study of Some Dynamic Stall Models," NASA TM 88917, March 1987.

[12]Carta, F. O., and Niebanck, C. F., "Prediction of Rotor Instability at High Forward Speeds, Vol. III, Stall Flutter," U.S. Army Aviation Material Labs. TR 68-16C, Feb. 1969.